Chapter 9

Applications of Remote Sensing in Geoscience

Hakim Saibi, Mohand Bersi, Mohamed Bodruddoza Mia, Nureddin Mohamed Saadi, Khalid Mohamed Saleh Al Bloushi and Robert W. Avakian

Additional information is available at the end of the chapter

http://dx.doi.org/10.5772/intechopen.75995

Abstract

Remote sensing is becoming an important and useful tool in mapping large, remote areas and has many applications in geosciences such as geologic and geo-structural mapping, mineral and water exploration, hydrocarbon exploration, natural hazards analysis, and geomorphology. The recent advances in remote-sensing imaging acquisition and availability of images can help geoscientists to explore and prepare maps quickly and evaluate the geo-potential of any specific area on the globe. Advances in remote-sensing data analysis techniques have improved the capacity to map the geological structures and regional characteristics and can serve in mineral exploration in complex and poorly understood regions. In this chapter, geophysical remotely sensed data (airborne geophysics) are integrated with other sources of remotely sensed data to analyze three separate areas, one each for geological structure, lineament presence and orientation, and geothermal potential. Three case studies are discussed in this chapter from three countries—Afghanistan, United Arab Emirates, and Algeria—to show the effectiveness of remote sensing in mapping and detecting geo-structural, geomorphological, and geothermal characteristics of ground surfaces.

Keywords: remote sensing, geological structures, geothermal exploration, remote areas

1. Introduction

Airborne remote sensing could be said to have started in 1858 when French balloonist Gaspard-Felix Tournachon took a photo of Paris from above. Sensors have ridden over time on balloons, to kites, to various aircraft, rockets, and finally on satellites. Sensor technology has come a long way from cameras and film, and we can now detect the entire useful electromagnetic spectrum, as well as gravity and magnetics themselves.

There are a number of advantages in using remote sensing. These include large existing databases such as Landsat and Satellite Pour l'Observation de la Terre (SPOT21); the ability to get regional views of large areas; ease of combining information from multiple sensors; no difficulty or danger in covering remote areas; availability of sophisticated computer analysis programs; a wide selection of energy bands (e.g., Infrared, ultraviolet, etc.) and of vital importance, low cost, and high speed.

Today's wide assortment of sensors allows interpreters to overlay, combine, or even subtract sensors in the search of meaningful maps. Spectral signatures of various plants and common rocks and minerals are well established, allowing remote reconnaissance to identify areas favorable for energy and mineral exploration or expand such areas through sensing techniques. This chapter shows only a small sample of what can be done with remote sensing, and the capabilities of these methods will only increase with time.

2. Application of remote sensing and remote geophysics to geological structural investigations in Aynak-Logar valley, Afghanistan

2.1. Introduction

The Aynak-Logar valley (ALV) is located around 30 km south of the capital city of Afghanistan (Kabul) (**Figure 1**). ALV is an area rich in cobalt, chromium, and copper, and other minerals (**Figure 2**). To detect the geo-structural features and understand their relationship with mineralization in this study area, remote-sensing and geophysical techniques were used.

Integrating remote-sensing and geophysical data has the potential to define the quantitative details of hitherto unknown areas and reduce the ambiguity of geological interpretation [1–5]. The results from remote-sensing and geophysical interpretation will support future mining exploration and development studies.

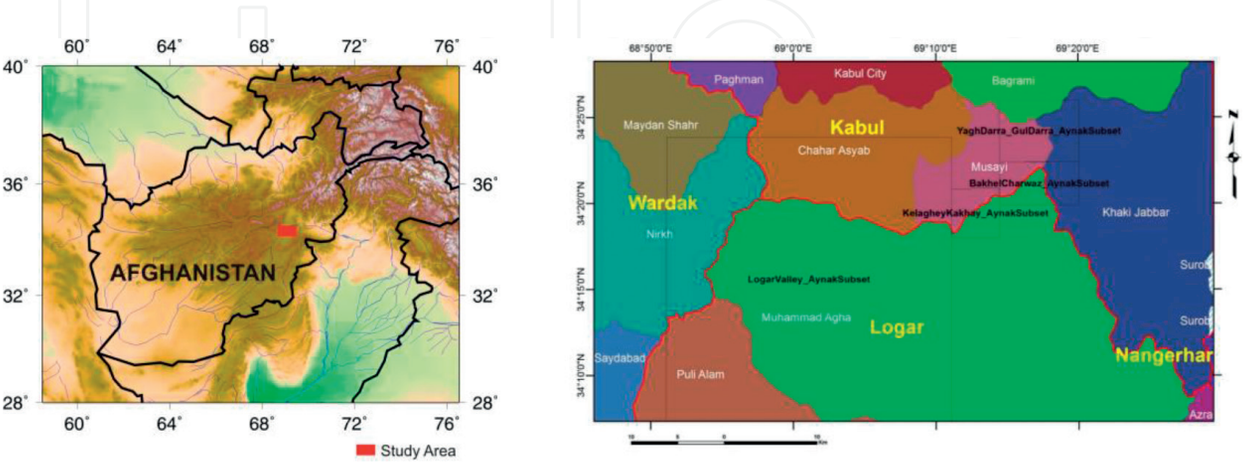

Figure 1. (left) Location of ALV study area in Afghanistan. (Right) ALV study area, red line shows the province boundary and the different districts as color coded.

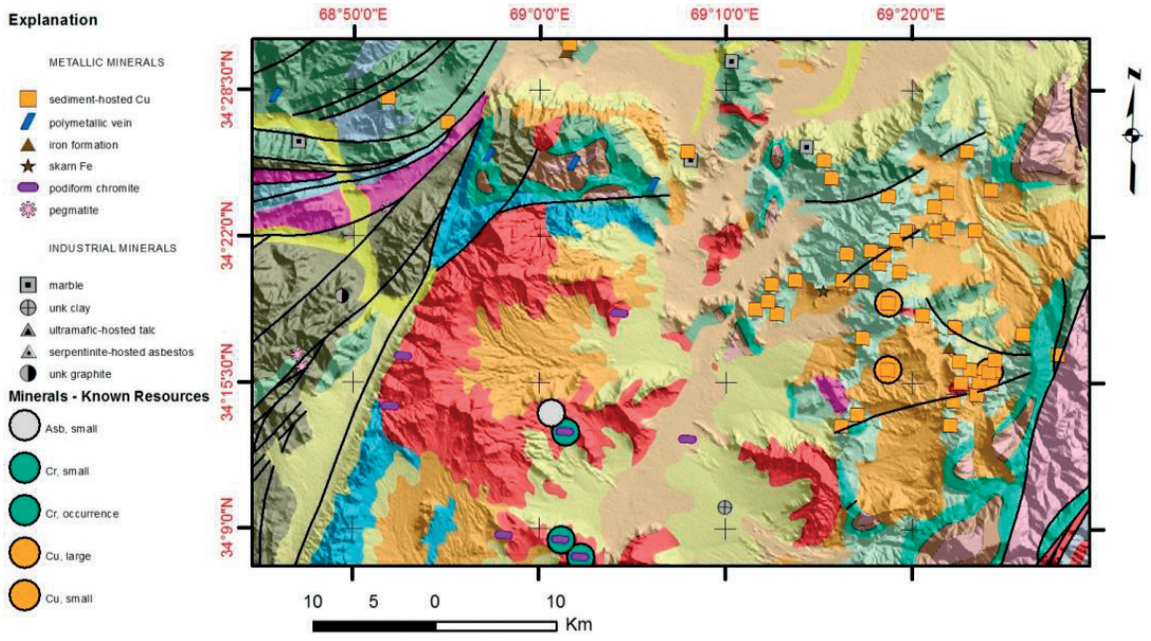

Figure 2. Map showing the mineral and structural information of the study area.

Geophysical data consist of aeromagnetic data obtained from the US Geological Survey (USGS) and processed using Geosoft Oasis Montaj Ver. 8. A magnetic survey is a powerful method to study the location of faults and other geological structures (dykes, intrusions) and is routinely applied in mining exploration surveys [6]. The remote-sensing data were processed using Earth Resource (ER) Mapper Ver. 7.

The Euler deconvolution (ED) method was applied to the aeromagnetic data with the objective of making geological features such as faults, contacts, and dykes more visible and of estimating their depth where possible.

Geologically, the exposed rocks in the core of anticline in ALV are metamorphic, mainly amphibolites, and gneiss, and belong to Welayati Formation (Fm). The Loy Khwar Formation overlies the Welayati Fm and is composed of metasedimentary sequences and hosts the copper mineralization in ALV.

Structurally, the Aynak-Logar Valley region is a pull-apart, post-orogenic basin resulting from the transpressive phase of two major sinistral shear faults, likely of Triassic age, trending in the NNE-SSW direction, while the main stress is in the NW-SE direction. The NW-SE compression causes on echelon folds in the NE-SW direction, with Triassic centers, sigmoidal in shape, and parallel to the edge of the major shear faults of NNE-SSW direction. This is due to the intensity of the deformation near the shear zone. The extension is represented by a NW-SE-oriented horst and graben structure that is the origin of the intrusion of ultramafic rocks into this region. The presence of normal faults at the boundaries of the horst and graben structures and their role in the intrusion of such rocks explain the presence of copper at the edges of these faults. The NE-SW faults are synthetic, with the major sinistral fault in the NNE-SSW direction. N-S faults are also synthetic to the major faults. During the Eocene,

NE-SW folds were created and present evidence of another deformational stage at that time but with NW-SE compression. The Pliocene-Oligocene forms an unconformity with Paleozoic and Triassic formations.

2.2. Materials and methods

2.2.1. Remote-sensing data

2.2.1.1. Landsat-enhanced thematic mapper plus (ETM+)

Landsat-7 was launched on April 15, 1999, from the Western Test Range aboard a Delta-II expendable launch vehicle. At launch, the satellite weighed approximately 2200 km. The spacecraft is about 4.3 m long and 2.8 m in diameter [7]. The Enhanced Thematic Mapper Plus (ETM+) instrument on board this spacecraft is an eight-band multispectral scanning radiometer (**Table 1**) capable of providing high-resolution imaging information of the earth's surface. It detects spectrally filtered radiation at visible, near-infrared, mid-infrared, and thermal infrared frequency bands from the sunlit earth in a 183 km-wide swath when orbiting at an altitude of 705 km ([7]). Nominal ground sample distances or "pixel" sizes are 15 m in the panchromatic band; 30 m in the 6 visible, near and mid-infrared bands; and 60 m in the thermal infrared band [7]. The satellite orbits the earth at an altitude of approximately 705 km with a sun-synchronous 98-degree inclination and a descending equatorial crossing time of 10 in the morning, with a repeat coverage interval of 16 days (233 orbits).

2.2.1.2. Shuttle radar topography mission

The Shuttle Radar Topography Mission (SRTM) obtained elevation data on a near-global scale to generate the most complete high-resolution digital topographic database of the Earth [8]. SRTM consisted of a specially modified radar system that flew onboard the Space Shuttle Endeavour during a 11-day mission in February of 2000. SRTM is an international project spearheaded by the National Geospatial-Intelligence Agency (NGA), National Aeronautics and Space Administration (NASA), the Italian Space Agency (ASI), and the German Aerospace Center (DLR). There are three resolution outputs available, including 1-km and 90-m spatial

	Wavelength (μm)	EM region	Spatial resolution
1	0.45–0.52	Blue	30 m
2	0.52–0.60	Green	30 m
3	0.63–0.69	Red	30 m
4	0.76–0.90	Near-infrared	30 m
5	1.55–1.75	Middle-infrared	30 m
6	10.40–12.50	Thermal infrared	60 m
7	2.08–2.35	Middle-infrared	30 m
8	0.52–0.90	Panchromatic	15 m

Table 1. Radiometric characteristics of ETM+ sensors.

resolutions for the world and a 30-m spatial resolution for the US. The Global Land Cover Facility (GLCF) serves the main USGS editions and has "enhanced" editions. It also provides editions in WRS-2 tiles to approximate Landsat scenes. In this study, the 90-m resolution SRTM (WRS-2) data (**Table 2**) were used to derive the topographic features of the study areas.

2.2.2. Aeromagnetic data

The aeromagnetic data for the Aynak region were acquired in 2006 and 2008 by the USGS and the Naval Research Laboratory (NRL) [9, 10]. Lines were spaced 4 km apart and were flown at heights of 5 km or more, which is higher than ideal. The aeromagnetic data were reduced to the pole (RTP) using a magnetic inclination of 48.74 and a declination of 2.01 degrees.

2.2.3. Data analysis and data integration

Two Landsat-Enhanced Thematic Mapper Plus (ETM+) images were used for analysis **(Figure 3**). Three types of contrast stretching were tested by using a mathematical function to map the pixel values to new, enhanced values: linear stretch, histogram stretch, and special stretch [11]. These methods were used to enhance the contrast between lithological units in the study area and enhance the printed geological map. The transformation technique Hue-Intensity-Saturation (HIS) was applied to differentiate rock units in ALV. The HIS components (blue, red, and green) were allocated, respectively, using ETM bands: 631, 743, and 763 [12]. The variance of the bands was calculated by the optimum index factor (OIF) method [13].

Edge enhancement was applied to the ETM+ image to detect edges, and then these enhancements were added back into the original images to increase contrast in the vicinity of an edge [14]. Individual panchromatic band (15 m) applications of the edge detection filter (Laplacian of Gaussian filter) were tested for lineament identification. Principal component analysis (PCA) was also applied to the ETM+ image to reduce the number of variables in the dataset, while retaining most of the original variability in the data.

PCA transforms the data into a set of uncorrelated random variables that capture all of the variance of the original dataset and assign as much variance as possible to the fewest number of variables. PCA is a very effective method for analyzing multispectral satellite imagery. PCA transforms the original image bands into uncorrelated output bands. PCA is often used

Satellite	**Sensor**	**Capture resolution**	**Pixel resolution**
Space Shuttle Endeavor	C-band and X-band	1 arc second	30 m
		3 arc second	90 m
		30 arc second	1 km
Scene Type	Scene Size		Projection
Degree	1 degree latitude × 1 degree longitude		Geographic
WRS-2	185 km × 185 km		UTM
Mosaic	Global		Geographic

Table 2. Sensor and product characteristics of SRTM data.

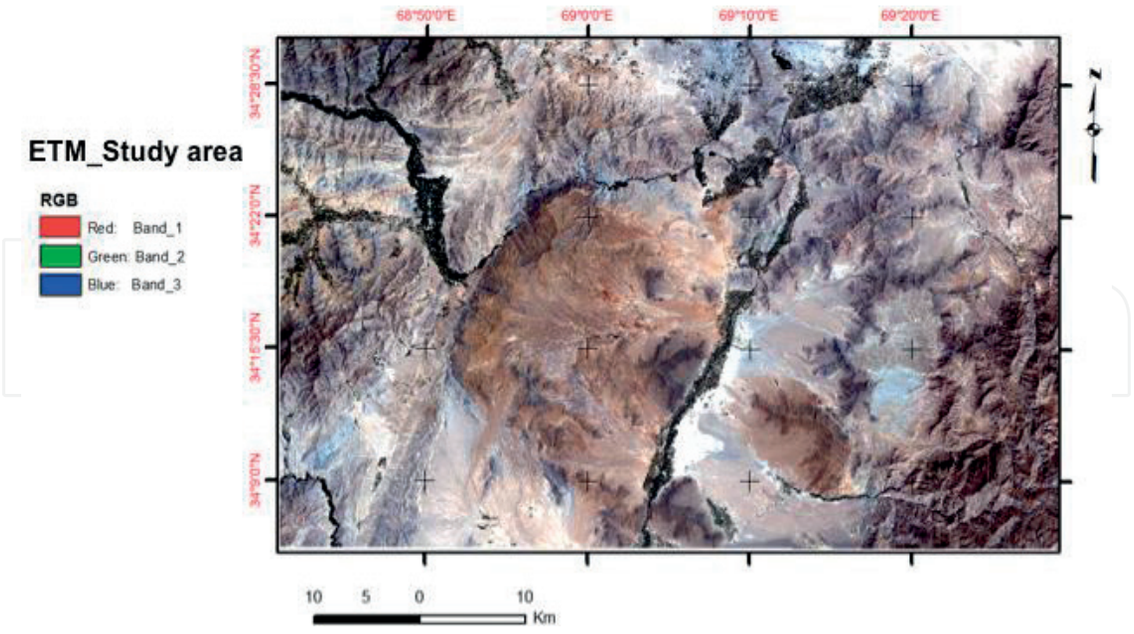

Figure 3. ETM map of the study area.

for dimensionality reduction and for creating color composite images with maximum information content. **Figure 4** shows the PCA map of the study area.

The Landsat ETM+ band combinations RGB-742 (red, green, blue) (SWIR-VNIR composite), RGB-543 (SWIR-NIR-VIR composite), and RGB-748 (SWIR-NIR-Panchromatic composite) were overlain on shaded relief maps to improve the possibility of lineament extraction [15]. The selected combinations have the advantage of preserving morphological features as well

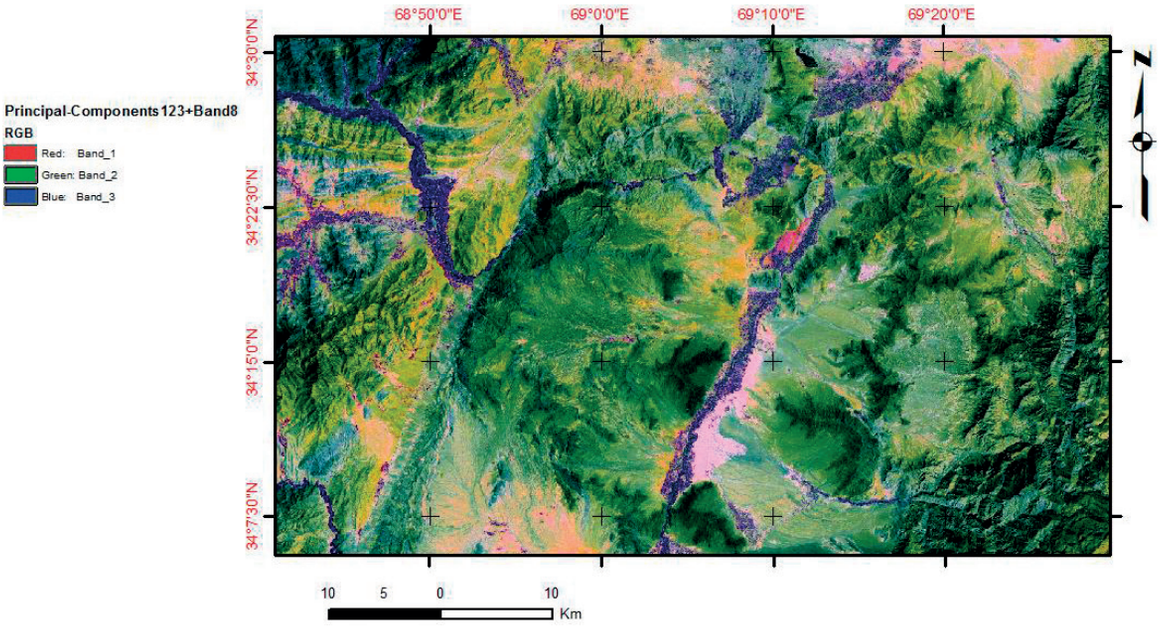

Figure 4. PCA map of the study area.

as displaying different lithological units in various colors because bands within the very near-infrared (VNIR) and shortwave infrared (SWIR) portions of the electromagnetic spectrum were used [16].

The shaded relief maps were used to simulate shading effects that were caused by the sun azimuth and elevation [17]. In this study, we experimented with an evaluation using an incoming illumination that is perpendicular to the prevailing trend of lineaments in the study area. Lineament identification has become increasingly valuable to structural recognition [18, 19].

Shaded relief maps were constructed from the SRTM Digital Elevation Model (DEM) by varying the azimuth and elevation of simulated sun illumination [20]. ETM+ VNIR color composites were overlaid on SRTM map to enhance lineaments identified in the ALV.

Lineaments were manually extracted based on photographic characteristics, such as shape (size, pattern, shadow, tone and texture) and geomorphologic features (fault-scarp, straight valley and drainage patterns).

The extracted lineaments were statistically analyzed to create rose diagrams and to evaluate differences in lineament direction and density. The analysis and interpretation of the extracted lineament lengths and trends, based on the age of the geological formations, provided useful information about the tectonic evolution of the study area.

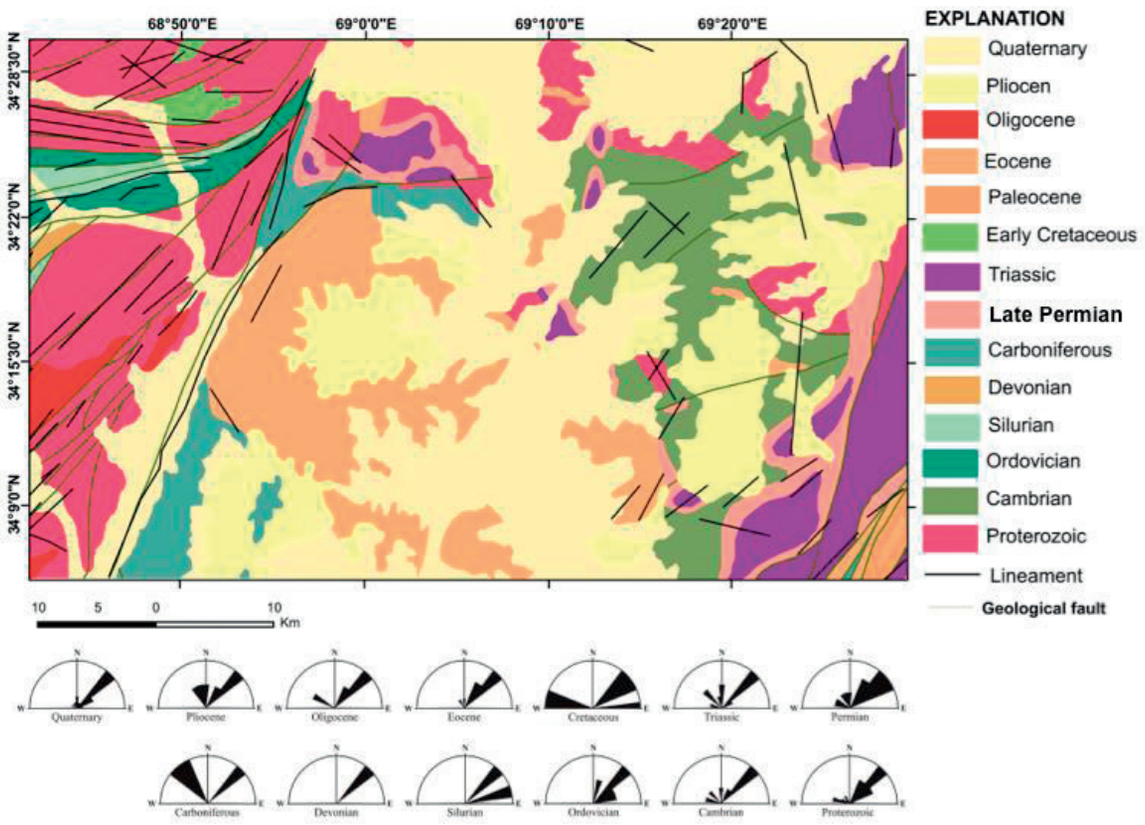

Figure 5. Geological map of the study area including the locations of geological faults [24–26] and interpreted lineaments from the remote-sensing data for the different geological ages from Proterozoic to Quaternary. The NE-SW geological-structural trend is present and the extracted lineaments run dominantly in the NE direction.

The aeromagnetic data were interpreted using Euler Deconvolution in order to determine the depth of geo-structural features (faults, contacts, dykes) and their location. The method was developed by [21, 22].

2.3. Results and discussions

Extracted lineaments were divided into 13 groups based on the age of the geological formations. The rocks of each geological age were classified as one unit and presented in one color group (**Figure 5**). The geological formations were cut by the extracted lineaments—Proterozoic, Cambrian, Ordovician, Silurian, Devonian, Carboniferous, Permian, Triassic, Cretaceous, Eocene, Oligocene, Pliocene, and Quaternary. Interpretation of these lineaments was based on the principle of crosscutting relationships [23]. The lineaments of each geological age were individually statistically analyzed to create rose diagrams. **Figure 6** presents the density map showing the location of lineaments from remote sensing. The interpreted faults from remote sensing are trending in the NE direction, which is in agreement with the trend of geological faults (**Figure 7**).

Figures 8 and **9** show the Euler solutions for a structural index (SI) of 0 and 1, respectively. The depths to the faults are ranging from 250 m to 2.5 km. The detected faults are located at borders of high magnetic anomalies and in agreement with the observed geological faults and interpreted remote-sensing geo-structural features.

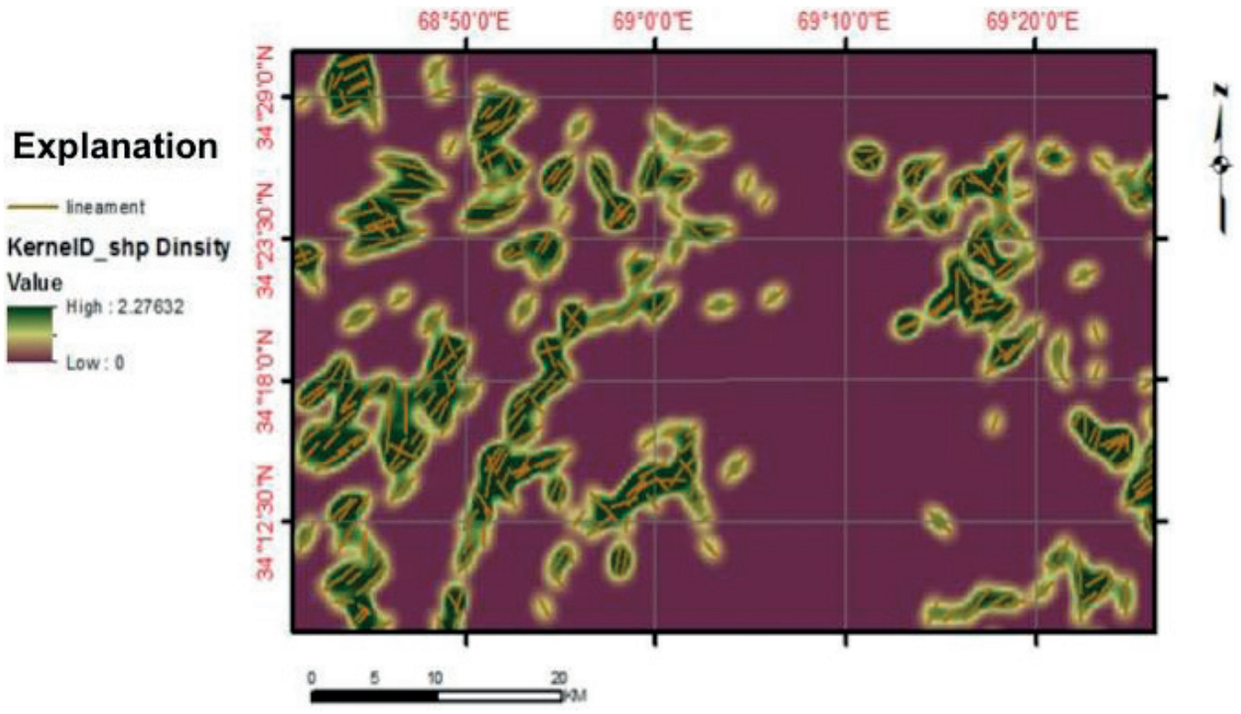

Figure 6. Lineament density map extracted from the shaded maps based on 30-m DEM data and natural-color Landsat imagery in the study area.

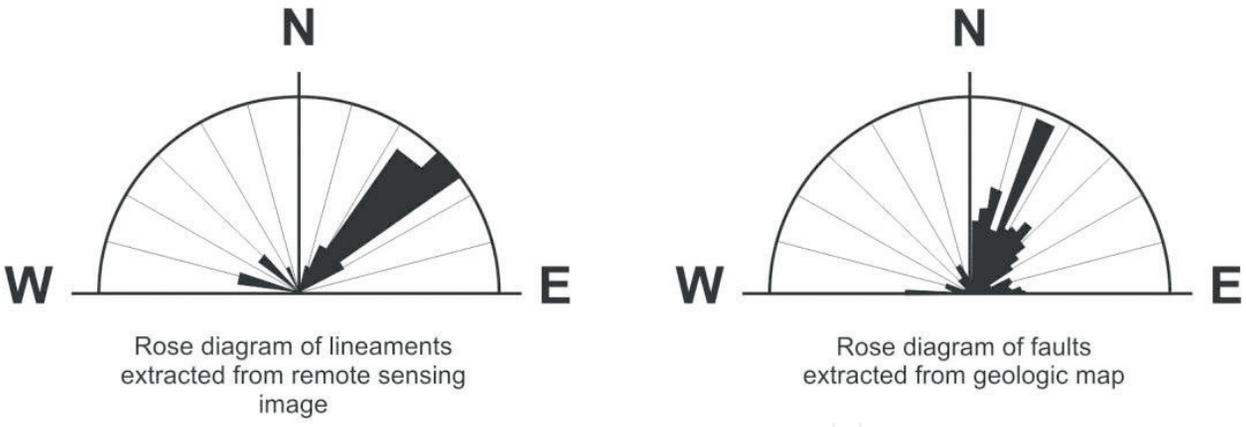

Figure 7. Rose diagrams extracted from geological map and shaded maps of the study area.

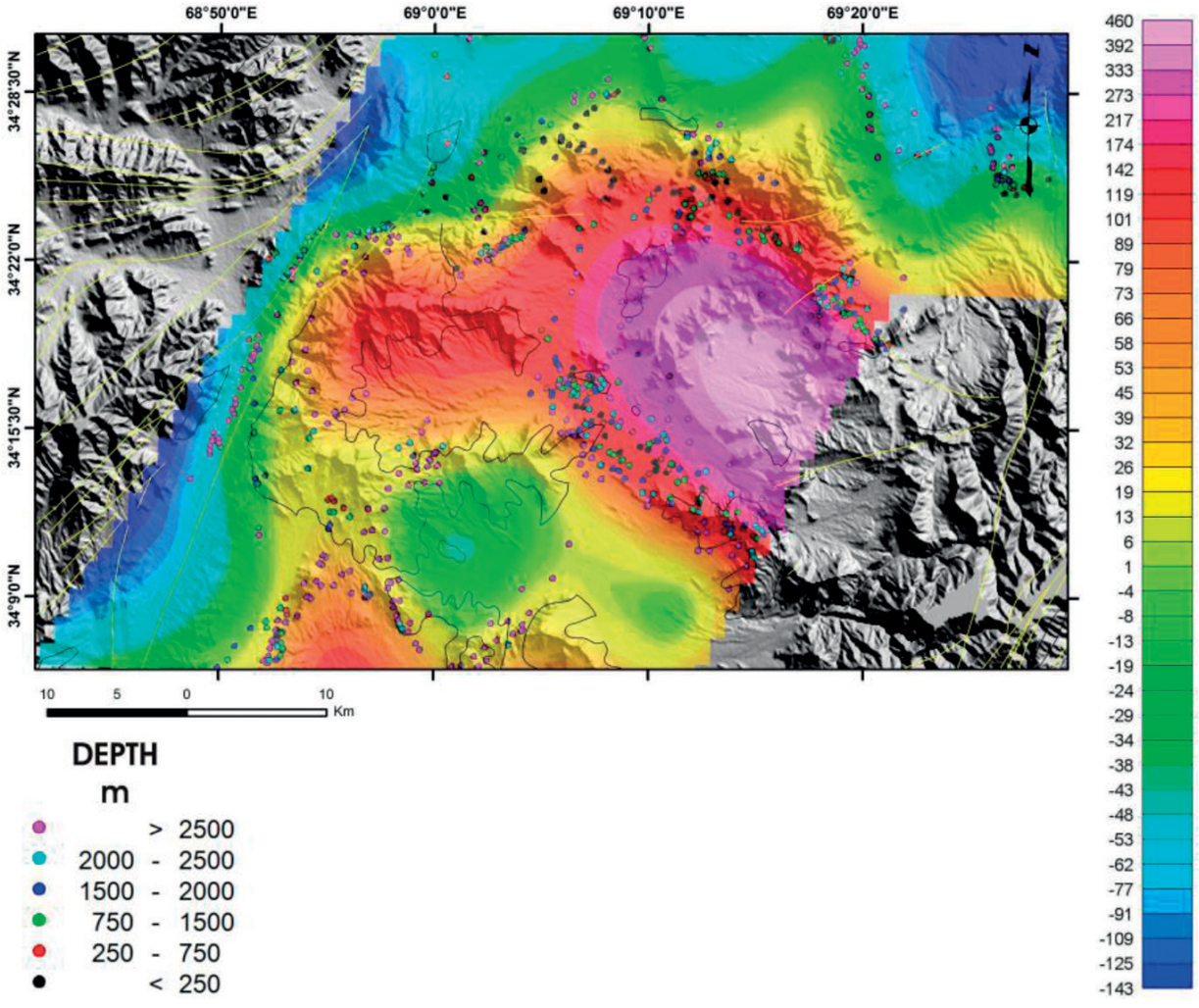

Figure 8. Euler deconvolution map of the study area with SI = 0. The background represents the RTP aeromagnetic map in nT overlaid on the SRTM map. Yellow lines represent geological faults.

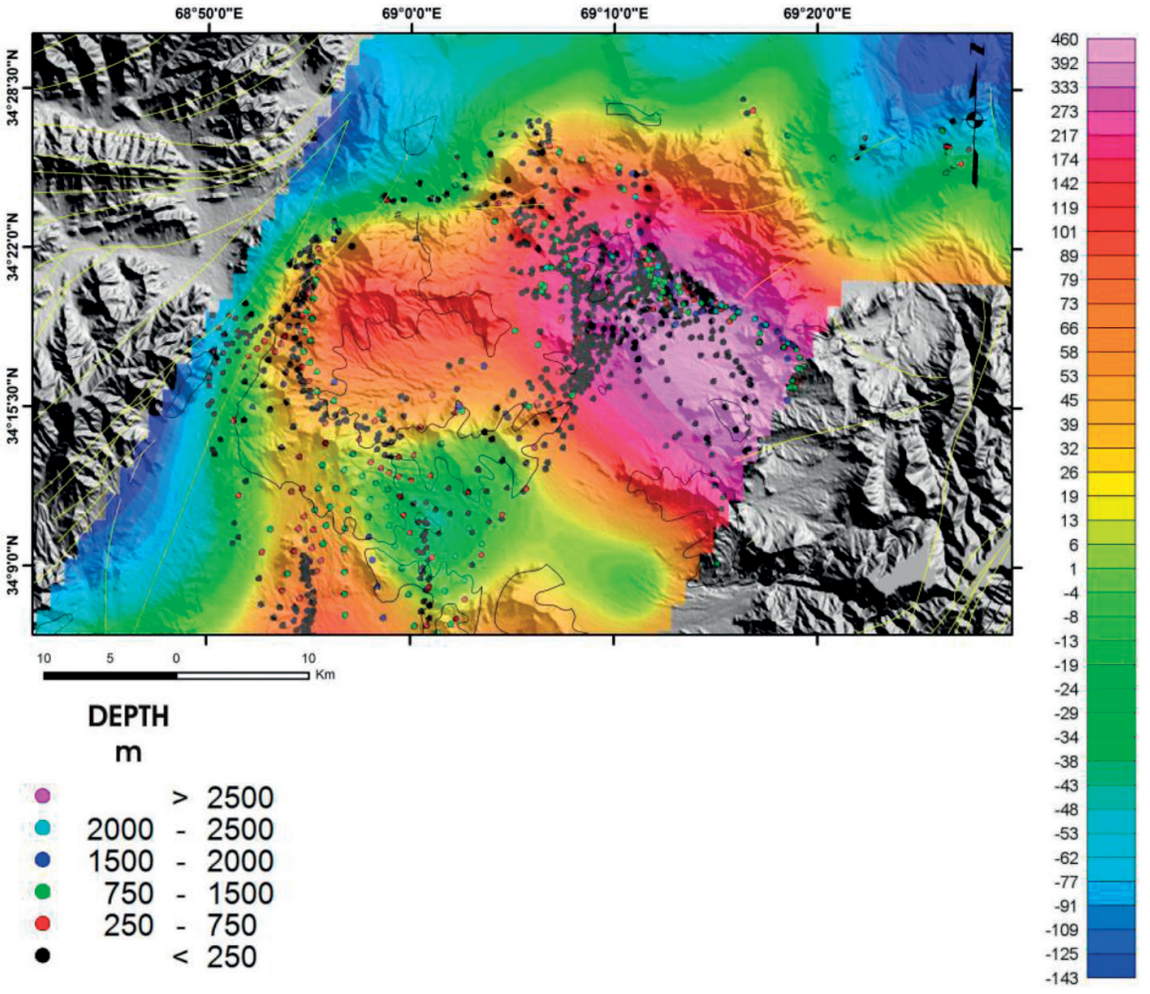

Figure 9. Euler deconvolution map of the study area with SI = 1. The background represents the RTP aeromagnetic map in nT overlaid on the SRTM map. Yellow lines represent geological faults.

3. Application of remote sensing in geothermal exploration: a case study at Mubazzarah Green Park hot spring area, Al-Ain city, United Arab Emirates

3.1. Introduction

Remote sensing is an essential technique for investigating geothermal ground, volcanic, or hot spring areas considering the unstable ground, and in this case, poor accessibility due to a national park. In addition, spatial analysis and repetitive monitoring of the thermal status can be done at lower cost than ground techniques. Satellite remote sensing offers the possibility to map land surface and vegetation variables in a thermal ground, volcanic, or hot spring areas such as hydrothermal altered minerals, land surface temperature (LST), emissivity, radiative heat flux (RHF) and land cover, and so on. [27]. Landsat satellite images (TM/ETM+) have a long history of use in volcano monitoring, considering hydrothermal alteration, heat flux, and thermal anomaly mapping over the whole world [28–35].

To provide a continuous monitoring of our environments, Landsat program launched a new satellite on February 11, 2013, that is, Landsat 8 with Operational Land Imager/Thermal Infrared Sensor (OLI/TIRS) sensors providing a total of 11 spectral bands: 9 OLIs and 2 TIRS bands. Landsat 8 sensors acquire images of both day and nighttime with a revisit time of 16 days for the same region. The OLI sensor collects data at 30-m resolution in visible, near-infrared, and shortwave infrared as well as a 15-m resolution panchromatic band. In addition, this sensor has a 30-m coastal aerosol band and 30-m cirrus band for cloud detection [36–38].

3.2. Materials and methods

In this case study, we applied the Landsat 8 Operational Land Imager (OLI)/thermal Infrared Sensor (TIRS) image to investigate the land use—land cover, emissivity, land surface temperature, and radiative heat flux of the Mubazzarah Green park hot spring area in Al-Ain city, United Arab Emirates (UAE) (**Figure 10**). The Landsat 8 OLI/TIRS image was acquired on December 1, 2016, and obtained from United States Geological Survey (USGS) archives free of cost. It has nine OLI bands of 30-m spatial resolution and two TIRS bands of 100-m spatial resolution. Land use-land cover (LULC) of the study area was mapped using Normalized Directional Vegetation Index (NDVI) value using the equation of $NDVI = \rho_{nir}\text{-}\rho_r/\rho_{nir} + \rho_r$; where ρ_{nir} is the reflectance of near-infrared band and ρ_r is the reflectance of the red band [27]. The NDVI value is a unitless ratio and ranges from +1 to −1. It is divided into four land cover classes: water body (NDVI <0), bared land/desert (NDVI = 0–0.2), mixed land (NDVI = 0.2–0.5) and vegetated (NDVI >0.5) [27]. The emissivity values in this region were calculated using the NDVI threshold method [39]. The Landsat 8 TIRS sensor has two thermal bands of 100 m in spatial resolution. We used band 10 of the sensor for land surface temperature estimation using the Mono-window algorithm [35, 39]. Radiative heat flux (RHF) was estimated by

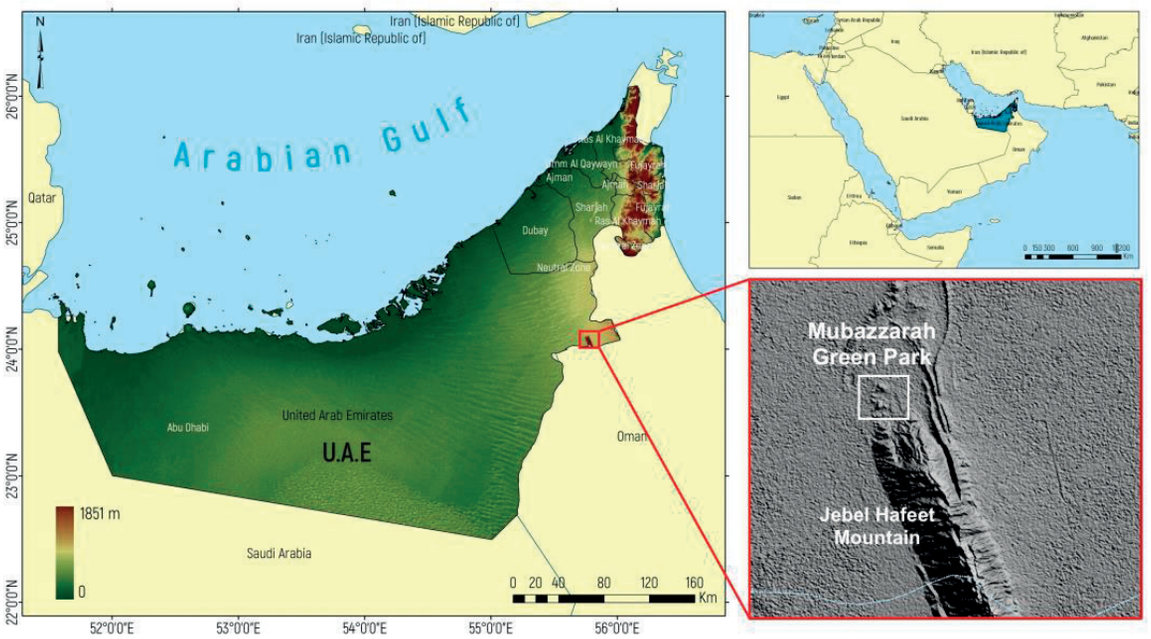

Figure 10. Location of study area.

using the Stefan-Boltzmann equation, that is, $Q_r = \tau\ \varepsilon\ A\ (T_s^4 - T_a^4)$, where Q_r = radiative heat flux (W/m^2), τ = atmospheric transmissivity, σ = Stefan-Boltzmann constant, ε = emissivity, A = area (m^2), Ts = land surface temperature (k), and Ta = ambient temperature (k) [27]. Meteorological data were collected from local meteorological station in the UAE including relative humidity (42%), ambient temperature (27°C), and so on. The atmospheric transmissivity during image acquisition was calculated using the NASA calculator. We obtained an atmospheric transmissivity of about 0.78 during the image acquisition of the study area.

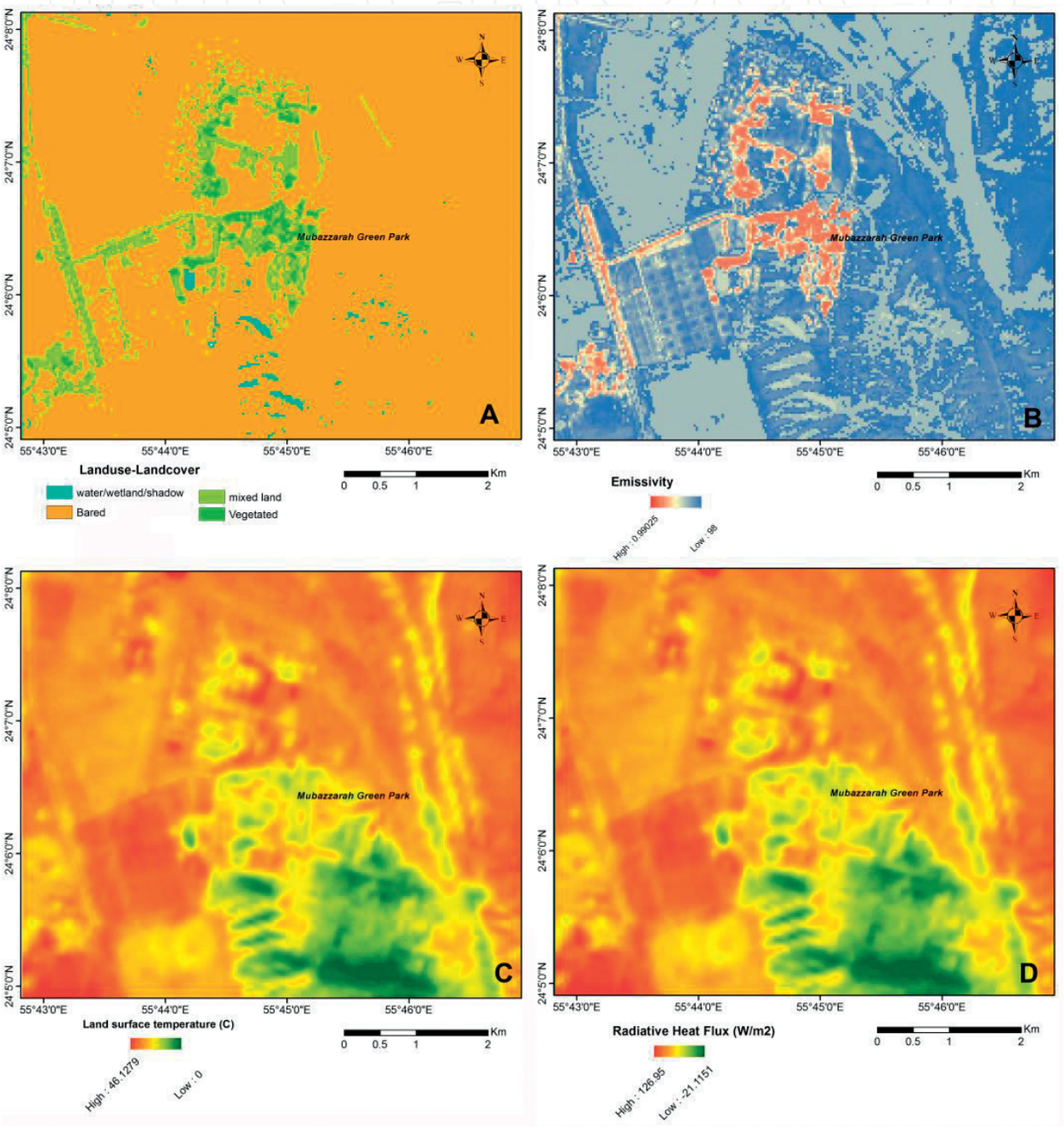

Figure 11. Remote-sensing application in the green Mubazzarah Park area in Al-Ain city, UAE. (A) LULC, (B) emissivity, (C) LST, (D) RHF.

3.3. Results and discussions

Total study area is the 43km^2 in and around the green Mubazzarah park area in Al-Ain City, UAE. The LULC result shows that the water bodies cover about 112 hectares, that is, 2.63% of the study area (**Figure 11A**). The largest LULC is the bare or desert land covering about 3721 hectares or 87.42% of the study area. The smallest LULC is the healthy vegetated region, which covers an area of about 59.4 hectares or 1.4% of the total study area. The mixed land, that is, the pixel area (30 × 30 m), contains some vegetation or some bare land or water, is present over about 364.14 hectares or 8.55% of the total study region (**Figure 11A**).

The calculated emissivity value ranges from 0.98 to 0.99025 for the land covers of this study area (**Figure 11B**). The highest land surface temperature (LST) obtained was about 46°C in the hot spring region of the green Mubazzarah Park shown as bright red color in the **Figure 11C**. The lowest LST was about 23.44°C shown as green color in the figure. We obtained the highest and lowest RHF of the study area, respectively, which was about 127 and − 21 W/m^2 using the Stefan-Boltzmann equation (**Figure 11D**). The calculated total radiative heat loss was about 1927 MW. The total heat discharge rate after multiplying the total RHL using the relationship coefficient (6.49) was about 12,507 MW. In conclusion, the study confirmed that the applied methods and images are adequate to explore and monitor (if possible) the thermal status of any geothermal area like this hot spring region with less time and low cost.

This is an ongoing experimental project. Ground truth data is not available at the time of writing. Ground truthing or accuracy assessment is an important part of remote-sensing applications; it may be added as part of further studies or developments.

4. Application of remote sensing in mining and geological investigations, case study: southern part of Algeria

This case study shows an example of the application of remote sensing to geological and mineralogical mapping of the Central Atlantic Magmatic Province (CAMP) formations in southern Algeria. Remote-sensing techniques such as principal component analysis (PCA), band ratios, band math, and target detection wizard can detect different mineral resources and interesting geological structures [40]. In this section, we present applications of different remote-sensing methods to map the mineral resources of the CAMP formations in southern Algeria using Landsat 8 OLI multispectral images. The remote-sensing analysis allows us to create a photo-lithological map of the study area presenting sills and dykes. The CAMP formations are associated to these large doleritic sills and long dikes.

4.1. General location and objectives of the study

The study area is located in the southwestern part of Algeria on the north flank of Tindouf basin (**Figure 12**). The north flank of the Tindouf basin contains two distinct regions. There is a high elevation region, which corresponds to the Hamada of Dra and a low elevation region situated in the Zemoul depression. The Zemoul depression is characterized by a steep relief, so a remote-sensing approach is the best way to map the CAMP outcrops in that region.

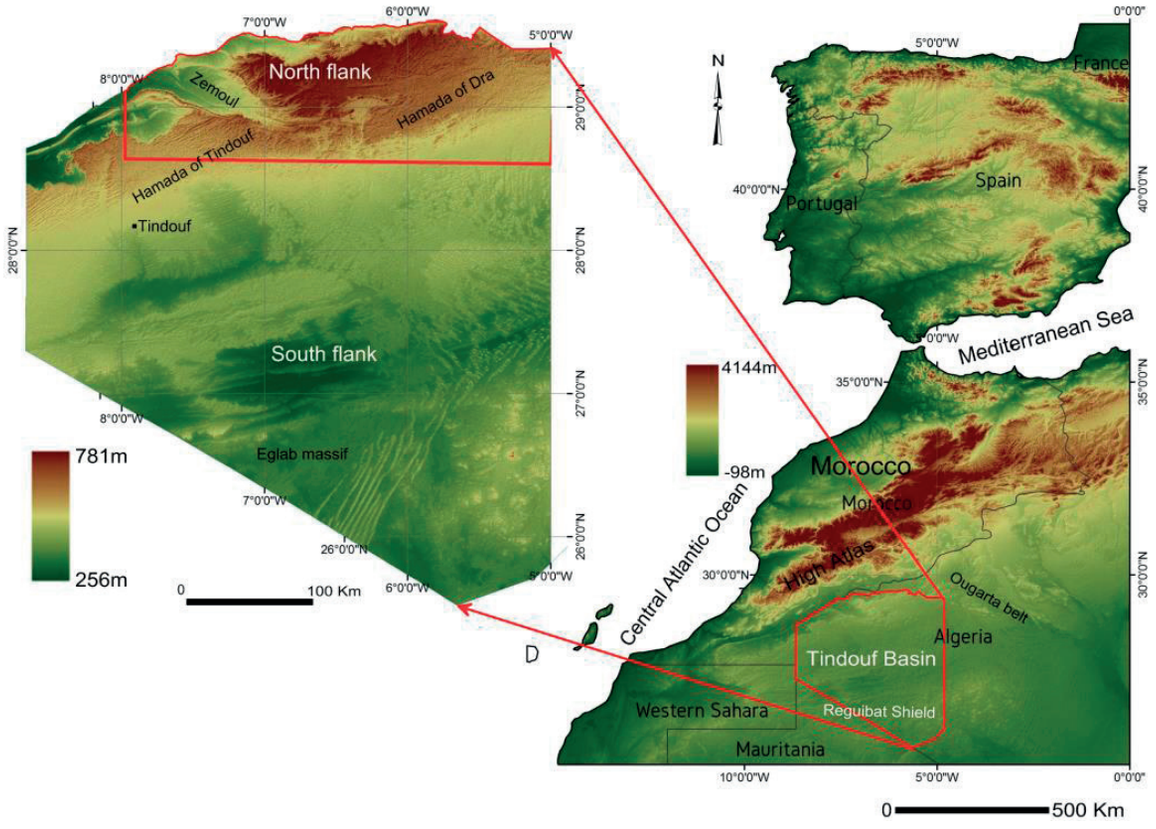

Figure 12. General location map of the study area.

4.2. Geological setting

The stratigraphic sequence in the study area consists of Paleozoic rocks [41, 42]. The main ages of the outcropping formations are Carboniferous and Devonian. The Carboniferous formations are mainly sandstone, while the Devonian formations are primarily clay sediments. The CAMP formation is in the form of doleritic sills and dykes, the most important mass of dolerites outcrop in the Devonian (**Figure 13**).

4.3. Remote-sensing analysis

The Operational Land Imager (OLI) multispectral images were used to enhance and highlight the geological and structural features in the study area. The image processing techniques such as band ratios, principal components analysis (PCA), target detection wizard, and band math have proved to be a strong tools for mapping geological features for mineral exploration purposes [40, 44].

4.3.1. Band ratios

Ratio is a powerful image processing technique, in that it allows discrimination between different lithological features. It is based on the division of the radiometric value of one band by the radiometric value of the same pixel of another band. The 7/1, 5/3, and 4/2 ratios have been selected to display in RGB mode (**Figure 14**).

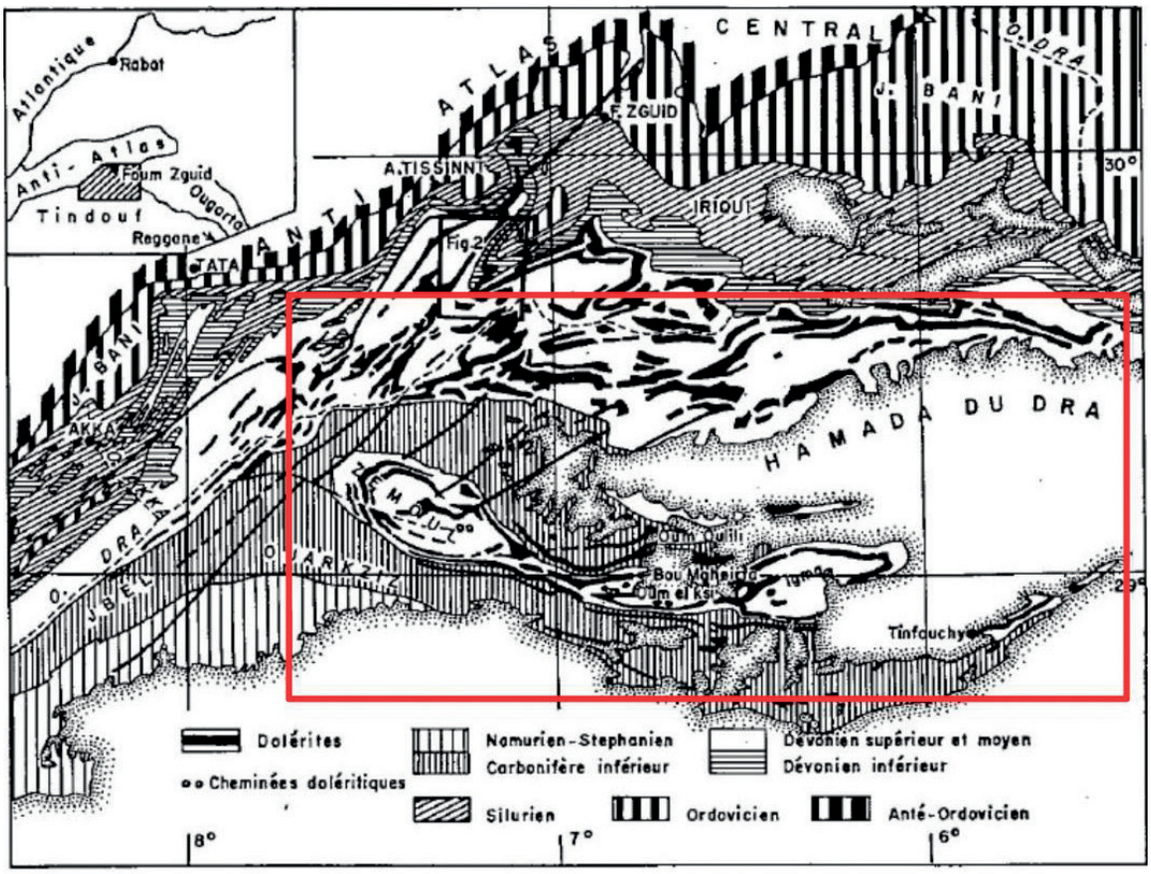

Figure 13. Geological map of the northern part of the Tindouf basin [43].

The ratio process highlighted the dolerites with dark green color; they are in the form of sills and long dykes. The Paleozoic are in shades of light green.

4.3.2. Principal components analysis (PCA)

The PCA technique is widely used in remote-sensing studies. The land cover reflectance in the OLI multispectral bands may present data redundancies, which can be avoided by using PCA analysis. It transforms an original correlated dataset into a substantially smaller set of uncorrelated variables that represents most of the information present in the original dataset [45]. The three first components, containing a large amount of information, were selected for RGB display (**Figure 15**).

The principal component analysis allows us to distinguish between different terrain aspects; the dolerites are in light yellow to white shades. The Paleozoic rocks appear in shades of magenta. This analysis shows that the intersection of the NE trending dykes with the center of the Zemoul antiform creates circular forms, which may correspond to the mineralization area.

4.3.3. Target detection wizard

The target detection wizard process allowed the detection of mineral targets by using specific algorithms such as adaptive coherence estimator (ACE) and spectral angle mapper (SAM).

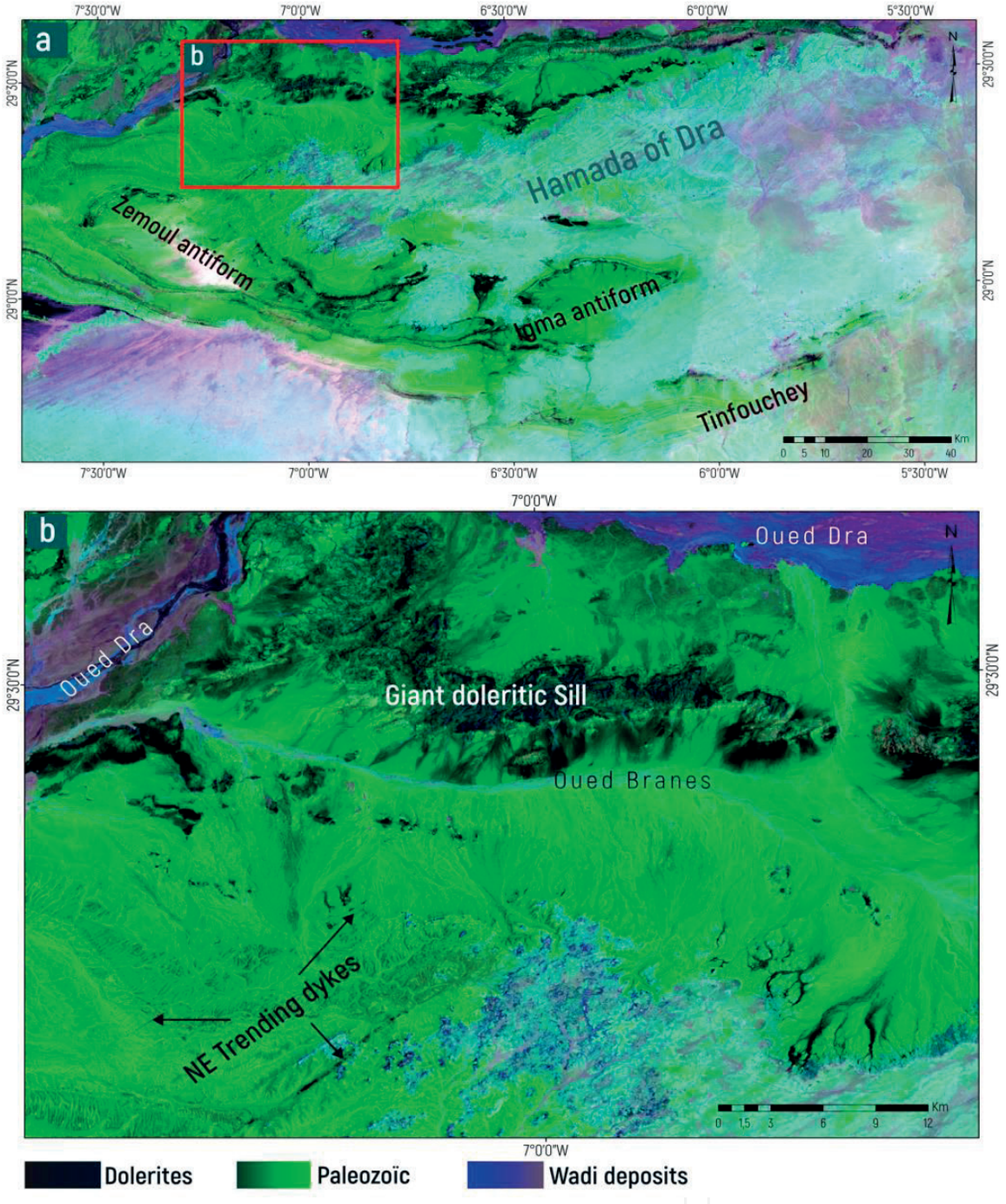

Figure 14. RGB display of 7/1, 5/3 and 4/2 ratios. (a) Regional area, (b) Focus area.

These methods have been proven able in geological target detection [46–50]. They are based on the spectral signature of rock-forming minerals, and they try to match image spectra to reference target spectra. The Anorthite was selected as a target lithology. The resulting image shows the distribution of non-altered sills. The target detection wizard analysis shows the high clinopyroxene dolerites, which are less altered than others, and may show good fracturation and structural indexes (**Figure 16**).

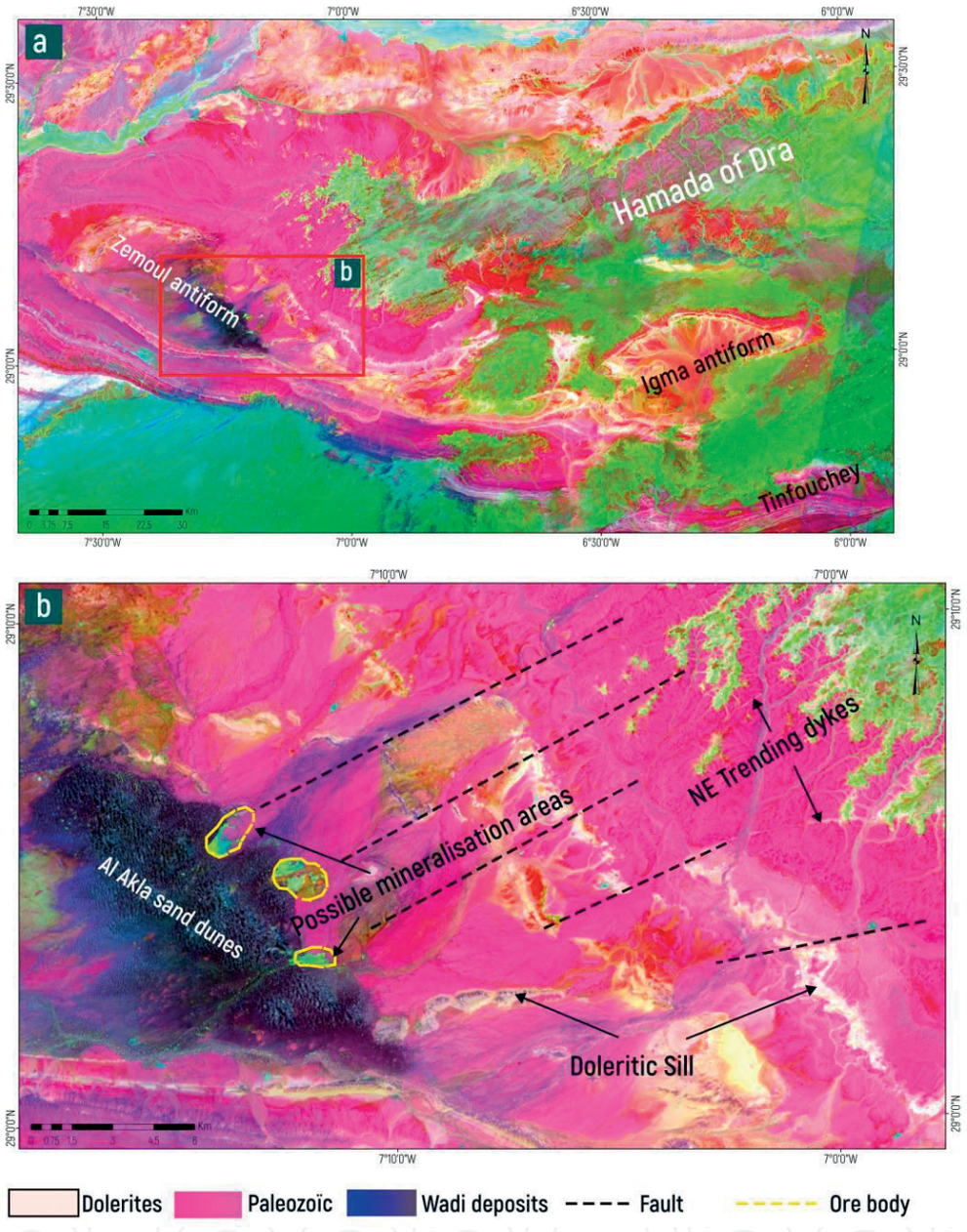

Figure 15. Three first components (PC3, PC2, and PC1) displayed in RGB mode, respectively.

4.4. Conclusions

Remote sensing in arid area such as the Tindouf basin has been proven to be a good tool for geological and mineralogical mapping. The use of advanced remote-sensing analysis allowed us to map dolerite outcrops, estimate their alteration and fracturation level, and then, extract the ore indexes and potentials. The results show that all dykes concentrate around Al Akla area, where some circular dolerite bodies have been detected. These circular bodies may correspond to a mineralized area. A lithostructural map of the study area has been created (**Figure 17**). This map can be used as a base map for the field validation mission.

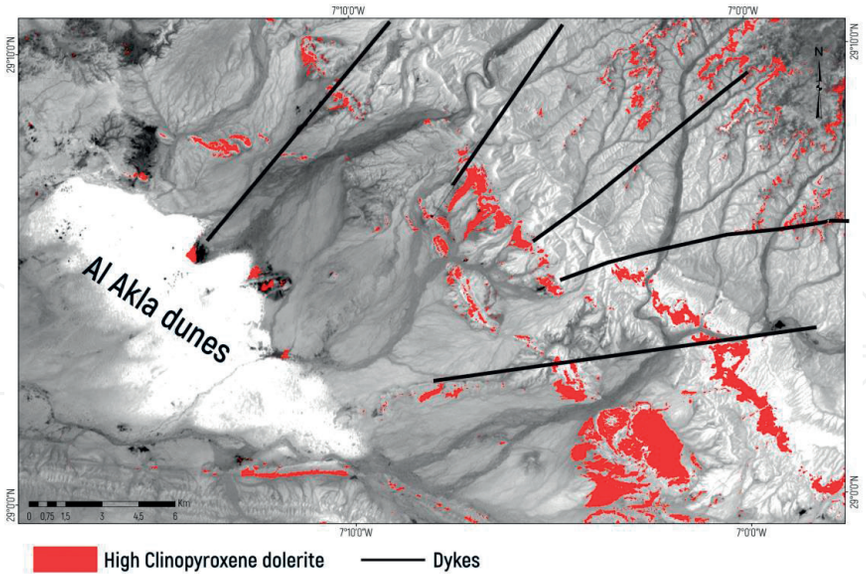

Figure 16. The target detection wizard results showing the high Anorthite content dolerites.

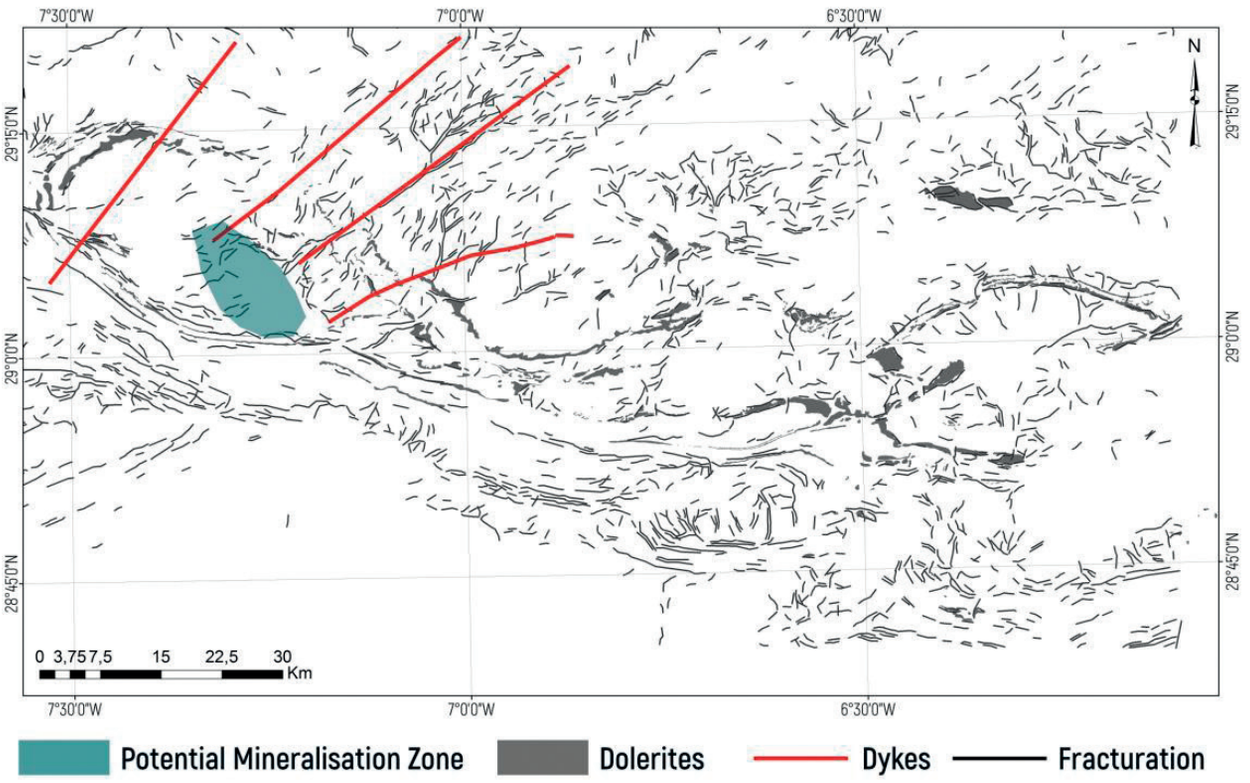

Figure 17. Photo-lithological map of the study area.

5. Conclusion

Here, we see a small bit of what can be done using remote sensing. As new sensors, such as Light Detection and Ranging (LIDAR) and new techniques like artificial intelligence (AI), come upon the scene, the potential for remote sensing will only grow. The modern interpreter will no

longer be hampered by maps of questionable quality in remote areas. They will be able to routinely assess the resources of vast, otherwise inaccessible areas quickly and effectively through the use of remote sensing.

Acknowledgements

The first author HS acknowledges the financial support of United Arab Emirates University (UAEU) by Research Start-Up Grant No. 8, Fund 31S264 (2016).

Author details

Hakim Saibi[1]*, Mohand Bersi[2], Mohamed Bodruddoza Mia[3,4], Nureddin Mohamed Saadi[3], Khalid Mohamed Saleh Al Bloushi[1] and Robert W. Avakian[5]

*Address all correspondence to: saibi.hakim@gmail.com

1 Department of Geology, College of Science, United Arab Emirates University, Al-Ain, United Arab Emirates

2 Department of Earth Sciences, Ferhat Abbas University, Setif, Algeria

3 Faculty of Engineering, Department of Earth Resources Engineering, Kyushu University, Fukuoka, Japan

4 Faculty of Earth and Environmental Science, Department of Geology, University of Dhaka, Bangladesh

5 Oklahoma State University Institute of Technology, USA

References

[1] Saadi NM, Aboud E, Saibi H, Watanabe K. Integrating data from remote sensing, geology and gravity for geological investigation in the Tarhunah area, Northwest Libya. International Journal of Digital Earth. 2008;**1**(4):347-366

[2] Saadi NM, Watanabe K, Imai A, Saibi H. Integrating potential fields with remote sensing data for geological investigations in the Eljufra area of Libya. Earth, Planets and Space. 2008;**60**:539-547

[3] Thurmond AK, Abdelsalam MG, Thurmond JB. Optical-radar-DEM remote sensing data integration for geological mapping in the afar depression, Ethiopia. Journal of African Earth Sciences. 2006;**44**:119-134

[4] Saibi H, Azizi M, Mogren S. Structural investigations of Afghanistan deduced from remote sensing and potential field data. Acta Geophysica. 2016;**64**(4):978-1003

[5] Mogren S, Saibi H, Mukhopadhyay M, Gottsmann J, Ibrahim EH. Analyze the spatial distribution of lava flows in Al-Ays Volcanic Area, Saudi Arabia, using remote sensing. Arabian Journal of Geosciences. 2017;**10**:133. DOI: 10.1007/s12517-017-2889-0

[6] Azizi M, Saibi H, Cooper GRJ. Mineral and structural mapping of the Aynak-Logar Valley (eastern Afghanistan) from hyperspectral remote sensing data and aeromagnetic data. Arabian Journal of Geosciences. 2015;**8**(12):10911-10918

[7] U.S. Geological Survey. Landsat 7, National Aeronautics and Space Administration. 1999. p. 32

[8] NASA. Available from: http://www2.jpl.nasa.gov/srtm/

[9] Ashan S, Hussain S, Kohistany AH, Shenwary GS, Mutty AS, Daud MA, Abraham JD, Anderson ED, Drenth BJ, Finn CA, Kucks RP, Lindsay CR, Phillips JD, Sweeney RE, Brozena JM, Ball DC, Childers VA, Gardner JM, Jarvis JL, Liang RT. Aeromagnetic survey in Afghanistan: U.S. Geological Survey Open-File Report 2007-1247. 2007

[10] Shenwary GS, Kohistany AH, Hussain S, Ashan S, Mutty AS, Daud MA, Wussow MD, Sweeney RE, Phillips JD, Lindsay CR, Kucks RP, Finn CA, Drenth BJ, Anderson ED, Abraham JD, Liang RT, Jarvis JL, Gardner JM, Childers VA, Ball DC, Brozena JM. Aeromagnetic surveys in Afghanistan: An updated website for distribution of data: U.S. Geological Survey Open-File Report 2011-1055. 2011. p. 8

[11] Mather PM. Computer Processing of Remotely-Sensed Images. 3rd ed. Chichester: Wiley; 2004

[12] Navulur K. Multispectral Image Analysis Using the Object-Oriented Paradigm. Boca Raton, CRC Press/Taylor & Francis; 2007

[13] Chavez PS, Berlin GL, Sowers LB. Statistical Methods for Selecting Landsat MSS. Florida, USA: CRC Press/Taylor and Frances Group; 1982

[14] Richards JA. Remote Sensing Digital Image Analysis, An Introduction. 2nd ed. Berlin: Springer; 1993

[15] Smith MJ, Clark CD. Methods for the visualization of digital elevation models for landform mapping. Earth Surface Processes and Landforms. 2005;**30**(7):885-900

[16] Sabins F. Remote Sensing Principles and Interpretation. New York: W.H. Freeman Company; 1997. p. 494

[17] Schowengerdt RA. Remote Sensing: Models and Methods for Image Processing. 3rd ed. London: Academic Press; 2007

[18] Yassaghi A. Integration of Landsat imagery interpretation and geomagnetic data on verification of deep-seated transverse fault lineaments in SE Zagros, Iran. International Journal of Remote Sensing. 2006;**27**:4529-4544

[19] Gloaguen R, Marpu PR, Niemeyer I. Automatic extraction of faults and fractal analysis from remote sensing data. Nonlinear Processes in Geophysics. 2007;**14**(2):131-138

[20] Singh AK, Parkash B, Choudhury PR. Integrated use of SRM, Landsat ETM+ data and 3D perspective views to identify the tectonic geomorphology of Dehradun valley, India. International Journal of Remote Sensing. 2007;**28**:2403-2414

[21] Thompson DT. EULDPH: A new technique for making computer assisted depth estimates from magnetic data. Geophysics. 1982;**47**(1):31-37. DOI: 10.1190/1.1441278

[22] Reid AB, Allsop JM, Granser H, Millett AJ, Somerton IW. Magnetic interpretation in three dimensions using Euler deconvolution. Geophysics. 1990;**55**(1):80-91. DOI: 10.1190/1.1442774

[23] Rowland SM, Duebendorfer EM. Structural Analysis and Synthesis. 2nd ed. Palo Alto: Blackwell Scientific Publications; 1994

[24] Abdullah S, Chmyriov VM. Geological Map of Afghanistan. Kabul/Afghanistan: Ministry of Mining and Industry of Democratic Republic of Afghanistan; 1977 scale 1:500,000

[25] Doebrich JL, Wahl RR, Ludington SD, Chirico PG, Wandrey CJ, Bohannon RG, Orris GL, Bliss JD. Geologic and mineral resource map of Afghanistan, U.S. Geological Survey Open-File Report 2006-1038. 2006

[26] USGS. Aeromagnetic and gravity surveys in Afghanistan: A website for distribution of data, U.S. Geological Survey Open-File Report, 2006-1204. 2006

[27] Mia MB, Bromley CJ, Fujimitsu Y. Monitoring heat flux using Landsat TM/ETM + thermal infrared data – A case study at Karapiti ('Crater of the Moon') thermal area, New Zealand. Journal of Volcanology and Geothermal Research. 2012;**235-236**:1-10

[28] Abdelsalam MG, Stern RJ, Berhane WG. Mapping gossans in arid regions with Landsat TM and SIR-C images: The Beddaho alteration zone in northern Eritrea. Journal of African Earth Sciences. 2000;**30**(4):903-916

[29] Madani A, Abdel Rahman EM, Fawzy KM, Emam A. Mapping of the hydrothermal alteration zones at Haimur Gold Mine Area, South Eastern Desert, Egypt using remote sensing techniques. Egyptian Journal of Remote Sensing and Space Science. 2003;**6**:47-60

[30] Yetkin E. Alteration mapping by remote sensing: application to hasanda-melendiz volcanic complex [MSc thesis]. Ankara, Turkey 97: Middle East Technical University; 2003

[31] Ramadan TM, Kontny A. Mineralogical and structural characterization of alteration zones detected by orbital remote sensing at Shalatein District, SE Desert, Egypt. Journal of African Earth Sciences. 2004;**40**:89-99

[32] Harris AJL, Lodato L, Dehn J, Spampinato L. Thermal characterization of the Vulcano field. Bulletin of Volcanology. 2009;**71**:441-458

[33] Mia MB, Fujimitsu Y. Mapping hydrothermal altered deposits using Landsat 7 ETM+ image in and around Kuju volcano, Kyushu, Japan. Journal of Earth System Science. 2012;**121**(4):1049-1057

[34] Mia MB, Bromley CJ, Fujimitsu Y. Monitoring heat losses using Landsat ETM + thermal infrared data: A case study in Unzen geothermal field, Kyushu, Japan. Pure and Applied Geophysics. 2013;**170**(12):2263-2271

[35] Mia MB, Nishijima J, Fujimitsu Y. Exploration and monitoring geothermal activity using Landsat ETM + images-a case study at Aso volcanic area in Japan. Journal of Volcanology and Geothermal Research. 2014;**275**:14-21

[36] Roy DP, Wulder MA, Loveland TR, Woodcock CE, Allen RG, Anderson MC, Helder D, Irons JR, Johnson DM, Kennedy R, Scambos TA, Schaaf CB, Schott JR, Sheng Y, Vermote EF, Belward AS, Bindschadler R, Cohen WB, Gao F, Hipple JD, Hostert P, Huntington J, Justice CO, Kilic A, Kovalskyy V, Lee ZP, Lymburner L, Masek JG, McCorkel J, Shuai Y, Trezza R, Vogelmann J, Wynne RH, Zhu Z. Landsat-8: Science and product vision for terrestrial global change research. Remote Sensing of Environment. 2014;**145**:154-172

[37] Mishra N, Helder D, Barsi J, Markham B. Continuous calibration improvement in solar reflective bands: Landsat 5 through Landsat 8. Remote Sensing of Environment. 2016;**185**:7-15

[38] Loveland TR, Irons JR. Landsat 8: The plans, the reality, and the legacy. Remote Sensing of Environment. 2016;**185**:1-6

[39] Qin Z, Karnieli A, Berliner P. A mono-window algorithm for retrieving land surface temperature fromLandsat TM data and its application to the Israel–Egypt border region. International Journal of Remote Sensing. 2001;**22**(18):3719-3746

[40] Bersi M, Saibi H, Chabou MC. Aerogravity and remote sensing observations of an iron deposit in Gara Djebilet, southwestern Algeria. Journal of African Earth Sciences. 2016;**116**:134-150

[41] Fabre J. Géologie du Sahara occidental et central. Tervuren: Musée Royal de l'Afrique Centrale; 2005

[42] Chabou MC, Sebaï A, Feraud G, Bertrand H. Datation 40Ar/39Ar de la Province Magmatique de l'Atlantique Central dans le Sud-Ouest algerien. Comptes Rendus Geoscience. 2007;**339**:970-978

[43] Hollard H, Schaer JP. Southeastern Atlantic Canada, northwestern Africa, and continental drift: Discussion. Canadian Journal of Earth Sciences. 1973;**10**(4):584-586

[44] Sabins FF. Remote sensing for mineral exploration. Ore Geology Reviews. 1999;**14**(3): 157-183

[45] Jensen JR, Lulla K. Introductory digital image processing: A remote sensing perspective. New Jersey, USA: Prentice-Hall, Englewood Cliffs; 1987

[46] Drake NA, Mackin S, Settle JJ. Mapping vegetation, soils, and geology in semiarid shrublands using spectral matching and mixture modeling of SWIR AVIRIS imagery. Remote Sensing of Environment. 1999;**68**(1):12-25

[47] Girouard G, Bannari A, El Harti A, Desrochers A. Validated spectral angle mapper algorithm for geological mapping: comparative study between QuickBird and Landsat-TM. Paper presented at the XXth ISPRS Congress, Geo-Imagery Bridging Continents; Istanbul, Turkey; 2004

[48] Khan S. Hyperspectral remote sensing for detection of natural hydrocarbon seeps. Asian Journal of Multidisciplinary Studies. 2016;**4**(2):1-10

[49] Li Q, Wei X, Zhang B, Yan S, Liu X. The spectral analysis and information extraction for small geological target detection using hyperion image. Paper presented at the International Conference on Earth Observation Data Processing and Analysis. Wuhan, China. 2008

[50] Li Q, Zhang B, Gao L, Lu L, Jiao Q. The identification of altered rock in vegetation-covered area using hyperspectral remote sensing. Paper presented at the 2014 IEEE International Geoscience and Remote Sensing Symposium (IGARSS). 2014

IntechOpen